Analysis of high-*n* dielectronic Rydberg satellites in the spectra of Na-like Zn XX and Mg-like Zn XIX

K. B. Fournier
Lawrence Livermore National Laboratory, P. O. Box 808, L-41, Livermore, California 94550, USA

A. Ya. Faenov, T. A. Pikuz, A. I. Magunov, and I. Yu. Skobelev
Multicharged Ions Spectra Data Center of VNIIFTRI, Moscow, 141570, Russia

F. Flora, S. Bollanti, P. Di Lazzaro, and D. Murra
ENEA, Dipartimento Innovazione, Settore Fisica Applicata, 00044 Frascati, Roma, Italy

V. S. Belyaev, V. I. Vinogradov, A. S. Kyrilov, and A. P. Matafonov
Central Research Institute of Machine Building, 4, Pionerskaya St., Korolev, Moscow Region, 141070, Russia

M. Francucci, S. Martellucci, and G. Petrocelli
INFM - Dipartimento di Scienze e Tecnologie Fisiche ed Energetiche, Università di Roma Tor Vergata, Via di Tor Vergata, 00133 Roma, Italy

(Received 23 February 2004; published 30 July 2004)

We have observed spectra from highly charged zinc ions in a variety of laser-produced plasmas. Spectral features that are Na- and Mg-like satellites to high-*n* Rydberg transitions in the Ne-like Zn XXI spectrum are analyzed and modeled. Identifications and analysis are made by comparison with highly accurate atomic structure calculations and steady state collisional-radiative models. Each observed Zn XX and Zn XIX feature comprises up to ≈2 dozen individual transitions, these transitions are excited principally by dielectronic recombination through autoionizing levels in Na- and Mg-like Zn^{19+} and Zn^{18+}. We find these satellites to be ubiquitous in laser-produced plasmas formed by lasers with pulse lengths that span four orders of magnitude, from 1 ps to ≈10 ns. The diagnostic potential of these Rydberg satellite lines is demonstrated.

DOI: 10.1103/PhysRevE.70.016406 PACS number(s): 52.25.Os, 32.30.Rj, 32.70.Fw, 32.80.Dz

I. INTRODUCTION

X-ray line profiles are an essential diagnostic of local conditions in high-temperature plasmas. Stark broadening of spectral lines is a sensitive probe of the local electron density [1,2]. Ultra-short-pulse lasers [3] have created a new regime of high-temperature, high-density plasmas [4–7]. Recently, Stark broadening of *K*-shell lines from buried aluminum targets has been used to diagnose ultra-short-pulse laser-produced plasma (LPP) densities and measure plasma-polarization shifts on He- and H-like resonance lines [8,9]. In Refs. [8,9] satellites to H- and He-like resonance lines are globally shifted an equal amount with the parent line. Other groups working with ultra-short-pulse laser-produced aluminum plasmas [10,11] have demonstrated that the effect of satellites near to the resonance lines can significantly distort the broadened line profiles and (potentially) affect the conclusions that are drawn from spectral analysis.

The Ne-like spectrum is the *L*-shell analog to the very useful He-like resonance lines. We have measured the *L*-shell Rydberg series in the Ne-like Zn XXI spectrum, and associated, intense Rydberg satellites from Na- and Mg-like Zn^{19+} and Zn^{18+}. The laser pulses in the present work are orders of magnitude longer than the ≈150 fs pulses in [7–11], but the establishment of the Rydberg satellite structure to the Ne-like spectrum is a crucial step toward having robust *L*-shell x-ray diagnostics in near-solid-density plasmas.

L-shell spectroscopic diagnostics have been proposed for and applied to diagnose conditions in inertial confinement fusion (ICF) plasmas [12] and pulsed power produced plasmas [13]. In both cases, the $n=3$ satellites to the principal $2p-3d$ Ne-like resonance lines are developed as a diagnostic of temperature and density conditions in the plasma. In the case of the ICF spectral diagnostics, relatively broad features from near-neonlike Xe ions are analyzed, the features comprise lines from F- to Mg-like ions [12]. However, in that case, where the temperature is not too high relative to the temperatures of equilibrium for the Na- and Mg-like ions, the intensity of 3C and 3D, and 4C, 4D lines, ($n\mathrm{C}:2p_{1/2}-nd_{3/2}$, $n\mathrm{D}:2p_{3/2}-nd_{5/2}$) could be overestimated due to the fact that Rydberg satellites lay inside the contour of thermally and Stark broadened Ne-like lines. In order that T_e and N_e are not overestimated when resonance lines are broad, careful, high-spectral-resolution observations should be done to determine the nature of the Rydberg satellites. In the case of recent *Z*-pinch experiments, spectral features from *L*-shell Mo ions are analyzed for their response to changes in plasma temperature, density and hot-electron fraction [13]. Again, Rydberg satellites could affect the shape of the principal Ne-like resonance lines, and should be characterized with high-spectral-resolution observations. However, to measure the influence of such Rydberg satellites to the 3C and 3D Ne-like lines is very difficult. At the same time it is well known that such Rydberg satellites radiated from Rydberg Na- and Mg-like autoionizing levels have two

different channels of decay: one that gives lines near the 3C, 3D lines and another that gives satellites near the Rydberg Ne-like lines. The second type of satellite lines can be very well resolved, and thus could be measured, modeled and used to facilitate the determination of the intensity of Rydberg satellites near 3C and 3D. In this paper, the $n=4$ and $n=5$ Rydberg satellites to Ne-like Zn XXI Rydberg transitions are observed in spectra from LPPs and modeled.

The *K*-shell Rydberg satellites of He-like resonance lines are an important *local* diagnostic of plasma conditions by themselves when the resonance lines are optically thick, as has also recently been shown. Local electron temperatures can be gauged without the complicating effects of line-of-sight integration if the autoionizing levels that give rise to the satellite lines are confined to the laser-target interaction region [14]. Using spatially resolved x-ray spectra from dense LPPs, essentially opacity-free and spatially-localized temperature diagnostics were established in [14]. For the spectra of the present work, the Rydberg series of Zn XXI lines are found to be optically thick for members with principal quantum numbers as high as $n=5$. Thus, the identification and classification of the *L*-shell Rydberg satellite emission of the present work has important diagnostic potential as an opacity free local measurement of conditions in the laser-target interaction region.

In order to have a robust *L*-shell diagnostic based on the Rydberg satellites to high-*n* Ne-like transitions, the spectral features must be identified and their behavior with plasma parameters characterized. In the present work, we have used high-spectral-resolution observations from three different LPPs to identify manifolds of Na- and Mg-like transitions. Detailed collisional-radiative (CR) calculations for the intensity of all transitions in each autoionizing manifold have been carried out. Our previous work [15] has identified Zn XXI lines up to $n=12$; in the present work we look at the Rydberg satellites that appear on both the red and blue sides of Ne-like features with $n \leqslant 7$. The behavior of the satellites relative to the Ne-like resonance lines as a function of temperature, accounting for opacity effects on all spectral lines, is shown. Thus, the two stated requirements for development of the diagnostic potential of these spectra are met: this is, to the best of our knowledge, the first attempt at modeling *L*-shell Rydberg satellite spectra at this level of detail.

II. EXPERIMENTAL SETUP

A. Laser-produced plasma facilities

The typical spectra for the very different lasers used in the present experiments (described below) are usually quite different in character [15,16]. However, for this article where we specifically want to understand the role of Na- and Mg-like satellites in x-ray spectra, we modified the laser parameters. The first laser described below was slightly defocused, and the second, the ps-length pulse laser, was strongly defocused. Thus, we could obtain in any laser-produced plasma (from 1 ps to 15 ns pulses and with laser wavelengths $\lambda_L=1.06-0.3$ μm) spectra where Rydberg satellites dominate.

The experimental setup and three facilities used in the present work are the same as recently described [15–17] elsewhere. Three laser-plasma facilities have been used to produce the spectra analyzed in this article. The first set of experiments was carried out in the Tor Vergata University of Roma (Italy). The laser source was a Quantel Nd:glass laser ($\lambda_L=1.055$ μm) delivering pulses with a maximum energy of 20 J and a temporal duration of 12–15 ns. A 20 cm focal-length doublet lens focused the laser beam on the target at a 45° angle of incidence. The spot size at best focus is ≈ 200 μm; for these experiments, the estimated beam diameter at the focal point was increased to ≈ 300 μm. In our experiments the laser energy was varied between 1 and 8 J, which allowed the laser intensity to reach $(0.1-1)\times 10^{12}$ W/cm^2.

The second set of experiments were carried out on the "Neodym" laser facility [18] at the Central Research Institute of Machine Building near Moscow. The laser energy was up to 1.0 J and the pulse duration in these experiments was kept to 1 ps. The fundamental wavelength of the Nd:glass laser ($\lambda_L=1.055$ μm) was used. The laser pulses are typically focused into a focal spot with diameter from 100 to 900 μm, yielding peak intensities from 10^{14} to 10^{17} W/cm^2; for these experiments, the intensity was kept to 10^{14} W/cm^2. It is known that this creates plasmas with mean electron temperatures ≈ 200 eV [16,18].

The third set of experiments was carried out at the ENEA "Hercules" laser facility in Frascati, Italy. This is a XeCl excimer laser with an active volume of $9\times 4\times 100$ cm^3 and an operating wavelength of 0.308 μm. The laser energy was 0.5–1 J, the pulse duration was 12 ns and the repetition rate was 0.5 Hz. The laser radiation was focused onto solid targets to form a spot 50–70 μm in diameter. Thus, the laser intensity on the target was about 10^{12} W/cm^2.

B. Targets and spectrometers

Stepped targets were used in all experiments. The heights of the steps were 300–800 μm. One part of the target contained zinc, while the second part contained Mg or Al, which produced spectral lines used for reference wavelengths. Between laser shots, the target was moved in the plane perpendicular to the laser beam to obtain spectra of the material investigated and reference materials on the same spectrograph film. The target step served to physically separate the two spectral images on the film.

X-ray spectra in the region 7.0–9.2 Å were obtained using focusing spectrometers with spatial resolution (FSSR-2D) [20–22]. Three different spectrometers were used: two of them have large aperture (15×50 mm) spherically bent ($R=150$ mm) mica and quartz (10-10) crystals, and one of them has a mica crystal with size 10×30 mm and a $R=100$ mm radius of curvature. The use of three different spectrographs increased the spectral range and spectral resolution that could be measured in the observations. Theoretical spectral resolution for the spectrometers varied from $\lambda/\Delta\lambda=3000$ up to $\lambda/\Delta\lambda=8000$. Because the wavelengths of all reference lines used are known with very good accuracy (better than 0.22 mÅ), the measurement accuracy for this

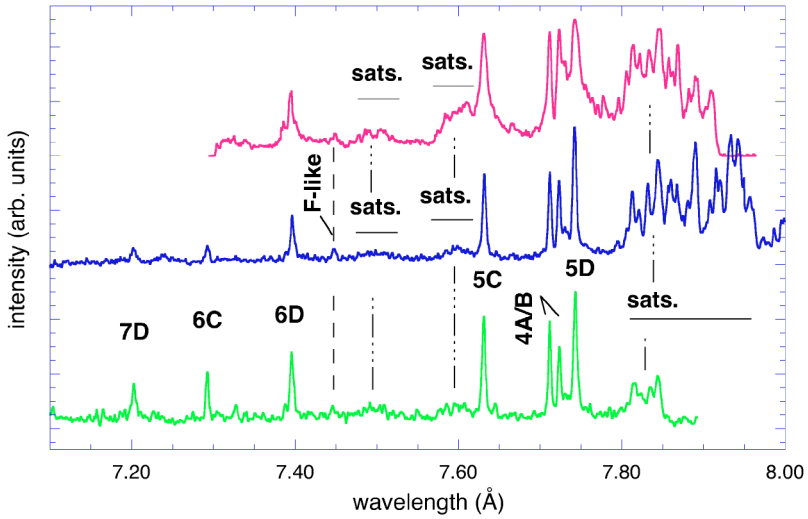

FIG. 1. Three examples of zinc high- *n* spectra measured from different plasma sources : top-12 ns XeCl laser, middle—12 ns Nd: glass laser, bottom—1 ps Nd: glass laser.

work was determined mainly by the width of line profiles and spectral line blending. As an example of the line broadening contributions considered, for the Ne-like 5C line at 7.6309 Å [15], we estimate $\Delta_{\mathrm{FWHM}}=1.26$, 1.13 and 2.94 mÅ linewidths from Doppler, natural and instrumental broadening, respectively. The Doppler width is computed for an ion temperature of 300 eV, the natural width accounts for both the radiative and collisional lifetimes of upper level and the collisional lifetime of the the lower level of the 5C transition, and the instrumental broadening assumes an instrumental

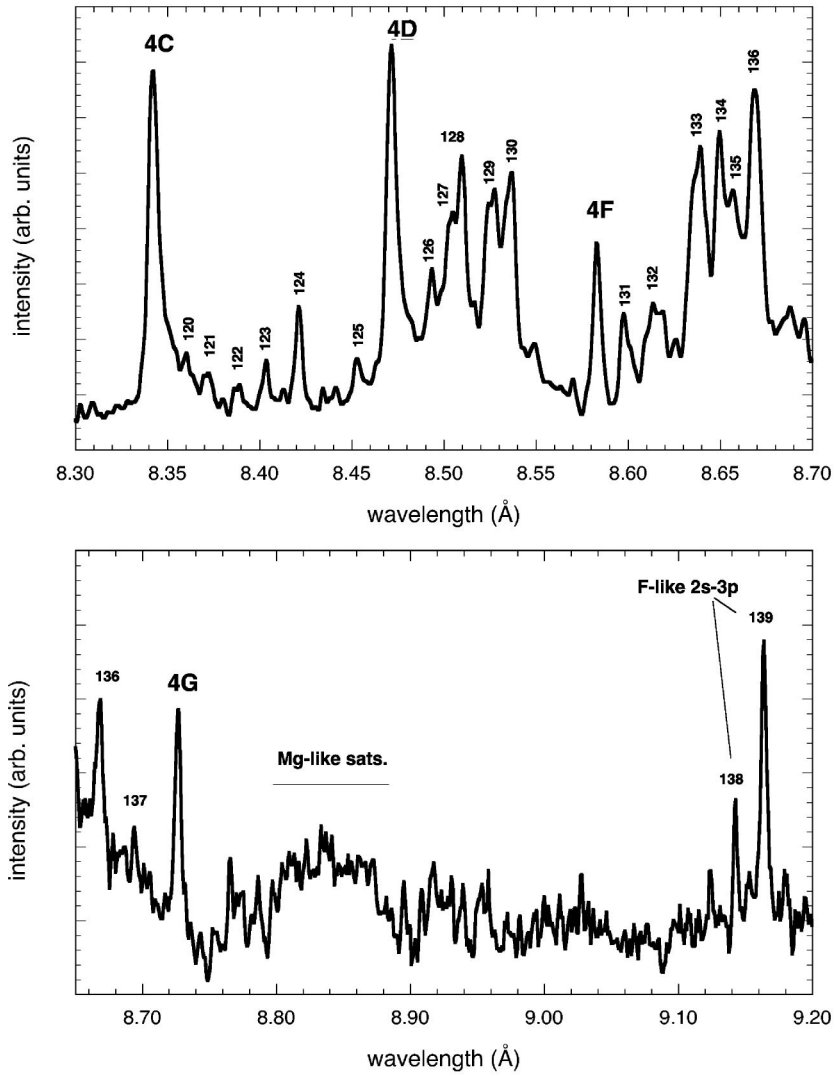

FIG. 2. Two spectra in the range of the $n=4$ Zn XXI resonance lines with strong dielectronic Rydberg satellites (top—12 ns Nd:glass laser, bottom — 12 ns XeCl laser).

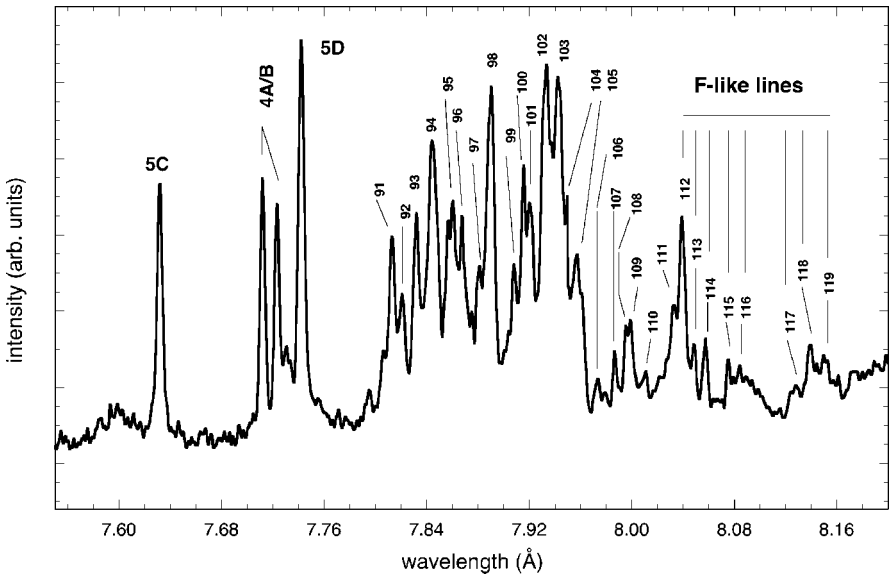

FIG. 3. Spectrum in the range of the $n=5$ Zn XXI resonance lines with strong dielectronic Rydberg satellites from a 12 ns Nd:glass LPP.

resolution of $\lambda/\Delta\lambda=2600$. We find that the relatively isolated 5C line in Fig. 3 is well fit by a Voigt profile computed with the above parameters.

When line profiles are symmetric, the positions of line centers can be measured with accuracies better than $0.1\times\Delta_{\mathrm{FWHM}}\approx 0.5$ mÅ. In some cases, when spectral lines are blended, line profiles are not symmetric and accuracies may be two to three times worse. It should be noted that generally speaking, the line center positions can be systematically shifted due to the Doppler effect caused by macroscopic plasma expansion. However, in the present experiments spectra were observed at angles $\approx 85°-90°$ to the plasma expansion axis. In this case, even for a plasma velocity $\sim 10^7$ cm/s systematic Doppler shifts must be smaller than 0.26 mÅ. Taking into account that reference lines are also shifted by the motion of the reference ions, we conclude that the systematic Doppler shift is three to ten times smaller than the expected measurement accuracy and, consequently, may be neglected. Thus, the overall accuracy of our wavelength measurements are about 0.5–1.5 mÅ. Because the high-resolution spectrographs can survey 0.3–0.7 Å in a single shot, some overlapping spectral regions were measured. Each region contained some of the reference lines with known wavelengths (spectral lines of He-like Mg XI and Al XII and previously measured lines of Ne-like Zn XXI [15]). Spectra were recorded on KODAK RAR 2492 film. The film holder was protected by two layers of 1 μm polypropylene filters coated with 0.2 μm layers of aluminum on both sides. Additional 2 μm polypropylene filters were used to stop plasma debris from reaching the surface of the crystal.

C. Observed spectra

Examples of measured spectra are shown in Figs. 1–3; the known response of the film has been taken into account. Figure 1 shows the Rydberg lines of Ne-like Zn^{20+} in the range 7.1–7.9 Å, the Ne-like features and the satellites of interest to the present work are labeled. This figure is similar to Fig. 5 in [15], in which lines from highly charged N-, O- and F-like Zn ions (Zn^{23+} to Zn^{21+}) are indicated in the data from a ps-length pulse LPP; these lines have been classified in [19]. The ps-length pulse LPP (bottom spectrum) here has

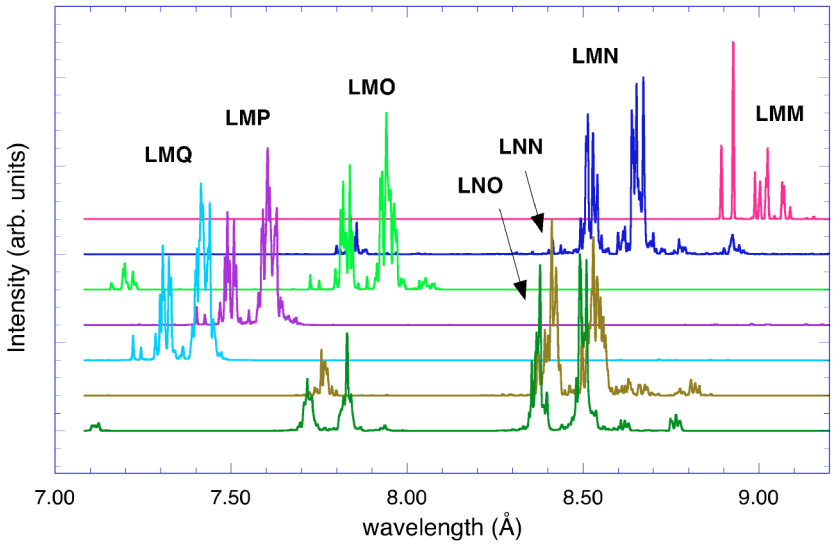

FIG. 4. (Color online) CR intensities of various DR channels in Na-like Zn XX (Zn^{20+} recombining to form Zn^{19+}).

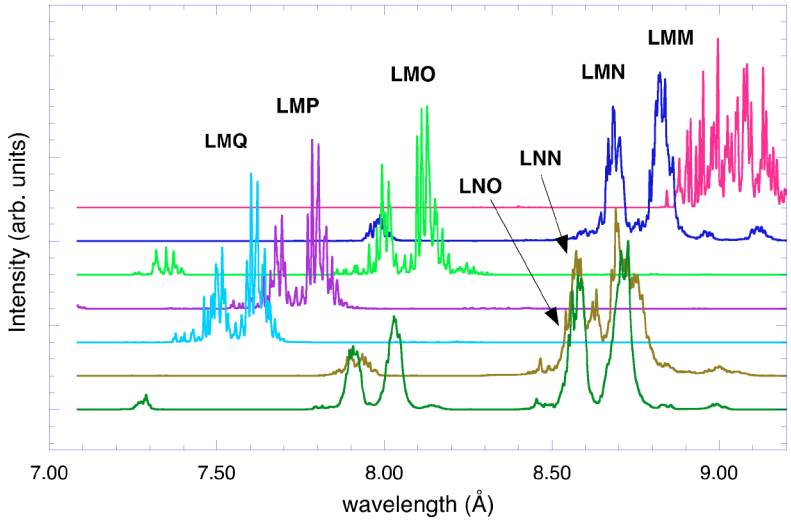

FIG. 5. (Color online) CR intensities of various DR channels in Mg-like Zn XIX (Zn^{19+} recombining to form Zn^{18+}).

been made by strongly defocusing the laser until the intensity on target was $\approx 10^{14}$ W/cm^2, far lower than what we would usually achieve [15,19]. The Rydberg satellites near the $n=5$ and $n=6$ lines in all three spectra have been indicated, showing the ubiquitous nature of the Rydberg satellites.

Figure 2 shows spectra in the range of the $n=4$ Zn XXI lines, along with strong satellite emission. The upper spectrum in Fig. 2 is from a 12 ns Nd:glass LPP and, as will be discussed below, has Zn XXI lines that are strongly affected by large optical depths. The lower spectrum is from a XeCl LPP, and shows lines from Mg-like DR satellites. Figure 3 shows a spectrum in the range of the $n=5$ Zn XXI lines, along with strong satellite emission. This spectrum, too, is from a 12 ns Nd:glass LPP and the Zn XXI lines are affected by large optical depths. The numbered features in Figs. 2 and 3 are listed in Table I with observed wavelengths [27]. Each Zn XX and Zn XIX feature in Figs. 2 and 3 comprises between six and ≈ 2 dozen nearly-equal-strength line transitions. Hence, tabulation of the individual components in each feature is impractical. Specific examples of a few observed transitions will be discussed below. F-like Zn XXII transitions that are coincident in wavelength with features 112– 119 in Fig. 3 have been identified in Table III note of Ref. [19].

III. SPECTRAL MODELS

A. Collisional-radiative models

Line identifications in the observed spectra are made by comparisons with CR transition intensities computed with the HULLAC suite of codes [23]. Details of our application of HULLAC data in CR models are given in Ref. [16]. All level structure and rate coefficients were calculated in intermediate coupling on a jj-coupled basis set. All level energies and rate coefficients have been entered into the CR rate matrix for the ions of the present work, and the resulting steady state level populations are then found. The rates of radiative decay (E1, E2, M1 and M2 transitions), collisional excitation and deexcitation, collisional ionization and three-body recombination, radiative recombination, autoionization and radiationless capture leading to dielectronic recombination (DR) have been considered. Charge states from the Mg-like to the N-like Zn have been treated. The steady state level populations are found according to

$$\frac{dn_j}{dt} = 0 = \sum_{i \neq j} n_i R_{i,j} - n_j \sum_{i \neq j} R_{j,i}, \tag{1}$$

where n_j is the population in level j, and $R_{i,j}$ is the rate at which population leaves level i and goes to level j. The resulting intensity for an observed line is given by

$$I_{j,i} = n_j A_{j,i}, \tag{2}$$

where $A_{j,i}$ is the total radiative transition rate between j and i.

We have included the effects of plasma self-absorption in our steady-state level population calculations with the escape factors approximation [24,25]. The escape factors ϵ suppress the radiative decay rates entered in Eq. (1)

$$A^{\text{eff}} = \epsilon A_{j,i}, \tag{3}$$

where A^{eff} is the effective transition rate in the presence of photon trapping and ϵ is the escape factor that depends on the atomic mass, the ion temperature and the plasma radius. For this work, we assume an isothermal, spherical plasma with a diameter ranging from 30 to 200 μm and an ion temperature $T_{\text{ion}}=T_e$; the choice of ion temperature has almost no effect on the computed self-absorption. Photon trapping redistributes the level population in the considered ions, particularly enhancing the population in the upper levels of strong transitions. The altered level populations mean that the absorption is different; the calculation is iterated until a self-consistent solution for the escape factors is reached. The enhanced level populations are redistributed by collisions, and in some cases, significantly enhance the emission in previously weak lines. Opacity strongly influences the relative intensities of the Ne-like Zn XXI features; this point is demonstrated in Sec. III C.

TABLE I. Measured wavelengths of Zn XX and Zn XIX satellite features, along with measured values of some Zn XXI and Zn XXII resonance lines. The calculated wavelengths of the satellite features are the centroid positions of the blended features from the CR model. The number in parentheses after the experimental wavelength is the measurement accuracy.

Key	Ion	Lower level	Upper level	J_l	J_u	λ_{calc} (Å)	λ_{exp} (Å)
5C	20	$2s^22p^6$	$2s^22p_{1/2}2p^4_{3/2}5d_{3/2}$	0	1	7.6275	7.6309(5)
4A	20	$2s^22p^6$	$2s2p^64p_{3/2}$	0	1	7.6970	7.7124(5)
4B	20	$2s^22p^6$	$2s2p^64p_{1/2}$	0	1	7.7099	7.7239(5)
5D	20	$2s^22p^6$	$2s^22p^2_{1/2}2p^3_{3/2}5d_{5/2}$	0	1	7.7387	7.7421(5)
91	19		LMO			7.8150	7.8130(5)
92	19		LMO			7.8262	7.8210(5)
93	19		LMO			7.8392	7.8320(5)
	and 19		LNO			7.8309	
94	19		LMO			7.8462	7.8460(10)
	and 20 (5G)	$2s^22p^6$	$2s^22p^2_{1/2}2p_{3/2}5s$	0	1	7.8427	
	and 18		LMP			7.8427	
	and 21	$2s^22p_{1/2}2p^4_{3/2}$	$2s^22p^4_{3/2}4d_{3/2}$	1/2	3/2	7.8482	
95	18		LMP			7.8591	7.8577(5)
96	18		LMP			7.8721	7.8686(5)
97	21	$2s^22p^2_{1/2}2p^3_{3/2}$	$2s^22p_{1/2}2p^3_{3/2}4d_{3/2}$	3/2	3/2	7.8818	7.8823(10)
	21	$2s2p^6$	$2s2p^1_{1/2}2p^4_{3/2}4d_{3/2}$	1/2	3/2	7.8841	
	21	$2s2p^6$	$2s2p^1_{1/2}2p^4_{3/2}4d_{3/2}$	1/2	1/2	7.8851	
98	21	$2s2p^6$	$2s2p^1_{1/2}2p^4_{3/2}4d_{5/2}$	1/2	3/2	7.8876	7.8886(5)
	21	$2s^22p^2_{1/2}2p^3_{3/2}$	$2s^22p_{1/2}2p^3_{3/2}4d_{3/2}$	3/2	5/2	7.8912	
	21	$2s^22p^2_{1/2}2p^3_{3/2}$	$2s^22p_{1/2}2p^3_{3/2}4d_{5/2}$	3/2	3/2	7.8944	
	21	$2s^22p^2_{1/2}2p^3_{3/2}$	$2s^22p_{1/2}2p^3_{3/2}4d_{3/2}$	3/2	1/2	7.8945	
99	19		LMO			7.9144	7.9095(5)
100	19		LMO			7.9238	7.9158(7)
101	19		LMO			7.9297	7.9202(7)
102	19		LMO			7.9402	7.9335(7)
103	19		LMO			7.9485	7.9420(7)
	and 21	$2s^22p^2_{1/2}2p^3_{3/2}$	$2s^22p_{1/2}2p^3_{3/2}4d_{3/2}$	3/2	5/2	7.9483	
	and 21	$2s^22p^2_{1/2}2p^3_{3/2}$	$2s^22p_{1/2}2p^3_{3/2}4d_{5/2}$	3/2	5/2	7.9519	
104	19		LMO			7.9543	7.9500(6)
105	19		LMO			7.9637	7.9573(6)
106	19		LMO			7.9826	7.9744(8)
	and 18		LMO			7.9778	
107	21	$2s^22p^2_{1/2}2p^3_{3/2}$	$2s^22p^2_{1/2}2p^2_{3/2}4d_{5/2}$	3/2	5/2	7.9901	7.9874(7)
108	18		LMO			7.9943	7.9950(6)
	and 21	$2s^22p_{1/2}2p^4_{3/2}$	$2s^22p_{1/2}2p^3_{3/2}4d_{5/2}$	1/2	1/2	8.0017	
109	21	$2s^22p_{1/2}2p^4_{3/2}$	$2s^22p_{1/2}2p^3_{3/2}4d_{3/2}$	1/2	3/2	8.0059	8.0015(6)
110	18		LMO			8.0131	8.0140(8)
	and 21	$2s^22p_{1/2}2p^4_{3/2}$	$2s^22p_{1/2}2p^3_{3/2}4d_{5/2}$	1/2	3/2	8.0188	8.0140(8)
111	18		LMO			8.0354	8.0358(8)
	and 19		LMO			8.0354	
112	21	$2s2p^6$	$2s2p_{1/2}2p^4_{3/2}4d_{3/2}$	1/2	3/2	8.0464	8.0398(10)
	21	$2s^22p^2_{1/2}2p^3_{3/2}$	$2s^22p^2_{1/2}2p^2_{3/2}4d_{5/2}$	3/2	5/2	8.0482	
113	21	$2s^22p^2_{1/2}2p^3_{3/2}$	$2s^22p^2_{1/2}2p^2_{3/2}4d_{5/2}$	3/2	1/2	8.0599	8.0489(10)
114	21	$2s^22p_{1/2}2p^4_{3/2}$	$2s^22p_{1/2}2p^3_{3/2}4d_{5/2}$	1/2	3/2	8.0692	8.0576(9)
	and 18		LMO			8.0613	
115	18		LMO			8.0813	8.0761(10)

TABLE I. (*Continued.*)

Key	Ion	Lower level	Upper level	J_l	J_u	λ_{calc} (Å)	λ_{exp} (Å)
116	21	$2s^22p_{1/2}^2 2p_{3/2}^3$	$2s^22p_{1/2}2p_{3/2}^3 4s$	3/2	5/2	8.0870	8.0849(6)
117	18		LMO			8.1283	8.1311(10)
118	21	$2s2p^6$	$2s2p_{1/2}^2 2p_{3/2}^3 4d_{5/2}$	1/2	1/2	8.1594	8.1405(10)
119	18		LMO			8.1518	8.1529(10)
4C	20	$2s^22p^6$	$2s^22p_{1/2}2p_{3/2}^4 4d_{3/2}$	0	1	8.3404	8.3420(6)
120	19		LNN			8.3594	8.3603(7)
121	19		LNN			8.3718	8.3720(11)
	19		LNO			8.3683	
122	19		LNN			8.3922	8.3892(13)
123	19		LNN			8.4118	8.4036(7)
124	19		LNN			8.4242	8.4212(8)
125	?						8.4526(8)
4D	20	$2s^22p^6$	$2s^22p_{1/2}^2 2p_{3/2}^3 4d_{5/2}$	0	1	8.4682	8.4715(7)
126	19		LMN			8.4942	8.4935(8)
	19		LNN			8.4978	
127	19		LMN			8.5093	8.5050(8)
128	19		LMN			8.5137	8.5088(6)
129	19		LMN			8.5279	8.5278(10)
	19		LNN			8.5297	
130	19		LMN			8.5412	8.5375(6)
	19		LNN			8.5404	
4F	20	$2s^22p^6$	$2s^22p_{1/2}2p_{3/2}^4 4s_{1/2}$	0	1	8.5807	8.5828(8)
131	19		LMN			8.5998	8.6003(7)
132	19		LMN			8.6193	8.6130(6)
133	19		LMN			8.6388	8.6410(6)
	and 18		LMN			8.6477	
134	19		LMN			8.6521	8.6500(7)
135	19		LMN			8.6582	8.6570(8)
	and 18		LMN			8.6627	
136	19		LMN			8.6716	8.6685(10)
	and 18		LMN			8.6690	
137	18		LMN			8.6854	8.6940(7)
4G	20	$2s^22p^6$	$2s^22p_{1/2}^2 2p_{3/2}^3 4s_{1/2}$	0	1	8.7251	8.7270(10)
138	21	$2s^22p_{1/2}^2 2p_{3/2}^3$	$2s2p_{1/2}2p_{3/2}^4 3p_{3/2}$	3/2	3/2	9.1134	9.1428(10)
139	22	$2s^22p_{1/2}2p_{3/2}^3$	$2s2p_{1/2}2p_{3/2}^3 3p_{1/2}$	2	2	9.1275	9.1635(10)
	and 21	$2s^22p_{1/2}^2 2p_{3/2}^3$	$2s2p_{1/2}2p_{3/2}^4 3p_{3/2}$	3/2	5/2	9.1280	

In what follows, simulated CR spectra are plotted on top of measured spectra. The synthetic spectra have been processed by taking the CR intensity for each line transition given by Eq. (2) and distributing the intensity over an appropriately normalized Voigt profile [26]

$$I(\nu) = \frac{1}{\sqrt{\pi}} I_{j,i} \phi(\nu), \tag{4}$$

where $\phi(\nu)$ is the line profile, which contains Doppler, natural and instrumental broadening terms. The line profile has the form

$$\phi(\nu) = \frac{a}{\pi} \int_{-\infty}^{\infty} \frac{e^{-y^2} dy}{a^2 + (u - y)}, \tag{5}$$

where $a = \gamma / 4\pi \Delta\nu_{tot}$, $\gamma = \Sigma A_{j,i} + \Sigma A_{j,f}^{AI} + \Sigma 2N_e Q_{j,f}^{CX}$ is the sum of the lifetimes of the upper and lower levels of a transition including radiative decay, autoionization and collisional destruction, respectively, $\Delta\nu_{tot} = (\Delta\nu_D^2 + \xi^2)^{1/2}$, where $\Delta\nu_D = (\nu_0/c)(2k_BT/M)^{1/2}$ is the Doppler width of the transition with central frequency ν_0, $\xi = \sqrt{2}\Delta/2.35$ is the Doppler width from the full width at half maximum (FWHM) Δ of a Guassian instrumental-response function, and u in Eq. (5) is the normalized frequency $(\nu - \nu_0)/\Delta\nu_D$. In every case, we have

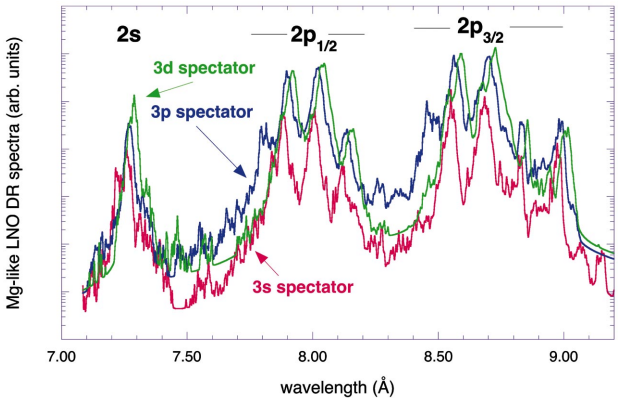

FIG. 6. (Color) CR intensities of the LNO DR channel in Mg-like Zn XIX (Zn^{19+} recombining to form Zn^{18+}). The calculations have been resolved based on the 3ℓ value of the spectator electron (3*s*—pink, 3*p*—blue, 3*d*—green).

used $T_i=150$ eV for Na- and Mg-like lines, $T_i=300$ eV for Ne- to O-like lines, radiative, autoionization and collisional lifetimes from our HULLAC data, and an instrumental function with a FWHM$=E/\Delta E=2600$. These parameters result in good fits to spectrally isolated lines in the Nd:glass 12 ns and 1 ps LPP spectra. In the case of the XeCl LPP spectra (top trace in Fig. 1), it is seen that there are broader red wings on the Zn XXI lines that may be due to greater opacity effects than we are accounting for, or due to the convergence of a larger series of higher-*n* Rydberg satellite manifolds than we have computed ($n\leqslant 7$ for the present work).

B. Dielectronic-recombination satellites

In what follows (Figs. 4–10) we show the calculated CR intensity for the Na- and Mg-like satellite spectra. Each Zn XX and Zn XIX satellite feature in Figs. 1–3 comprises between 6 and ≈24 lines, we refer to the gross features by the nomenclature used for manifolds of Auger transitions, which are the inverse channel for DR events. That is, in the figures that follow, a Zn XX or Zn XIX feature is given a designation of the form LMn'' or LNn'', where the first character indicates a promotion of an $n=2$ electron, the second character indicates that the electron has gone into the $n'=3$ (M) or $n'=4$ (N) shell, and the n'' designates the principal quantum number into which a free electron has been captured ($n''=3,\ldots,7$, M to Q, respectively). In our calculations, the full spectrum of DR channels has been treated as completely as possible: that is, for Na-like LMN features, promotions to all available $n'=3$ orbitals ($3\ell,\ell\leqslant 2$) have been allowed, and captures into all $n''=4$ orbitals ($4\ell,\ell\leqslant 3$) have been allowed. In the case of the Mg-like LMN DR channels, the capture from the initial Na-like configuration is allowed to proceed from any excited Na-like state with an occupied $n=3$ orbital; that is, DR channels proceed through states of the form $2(s,p)^7 3\ell 3\ell' 4\ell''$, with ℓ, $\ell'\leqslant 2$, and $\ell''\leqslant 3$. Thus, for example, a Zn^{18+} DR event can proceed as

$$2s^2 2p^6 3d + e \rightarrow 2s^2 2p^5 3d^2 4d \rightarrow \begin{cases} 2s^2 2p^6 3d4d + h\nu \\ 2s^2 2p^6 3d^2 + h\nu', \end{cases} \quad (6)$$

where e is an initial, free electron and $h\nu$ ($h\nu'$) is a photon produced by a $3d\rightarrow 2p$ ($4d\rightarrow 2p$) decay. Stabilization to Na- and Mg-like levels below the first ionization energy has been allowed via decays of any $n'=3$ or $n''=4$ electron. The same comments apply for the LNN and LNO DR channels, in which the promoted electron goes to any $n'=4$ orbital, and the capture of the free electron is into either $n''=4$ or 5. For LNn'' DR from Na-like Zn^{19+} to Mg-like Zn^{18+}, an initial spectator electron is allowed in any $n=3$ orbital. For the LMn'' channels, all orbitals with $\ell\leqslant n''-1$ have been included, for the LNn'' channels, all orbitals with $\ell\leqslant 4$ have been included.

The emissivity $\varepsilon_{\mathrm{DR}}$ of a Na- or Mg-like Rydberg satellite excited by DR can be expressed as

$$\varepsilon_{\mathrm{DR}} = N_e N_{q+1} F_1(T_e) F_2(j,f), \quad (7)$$

where N_e is the free-electron density (assumed to have a Maxwellian distribution of energies), N_{q+1} is the density of

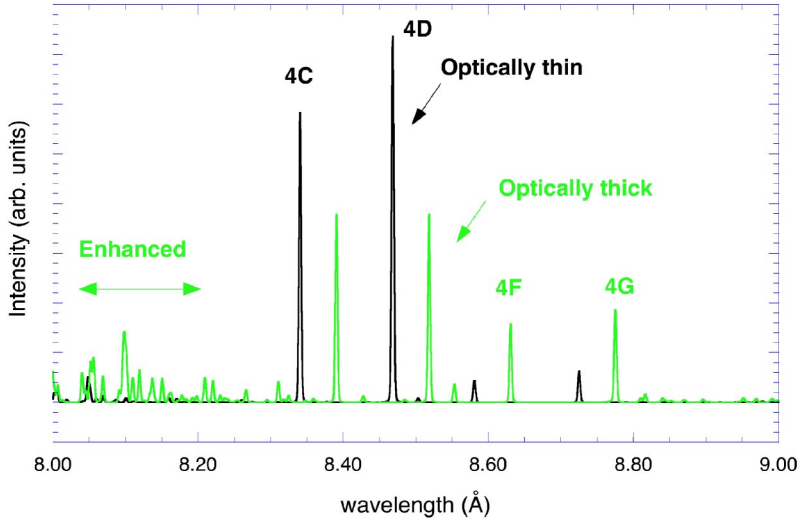

FIG. 7. (Color online) O-, F- and Ne-like spectra computed with and without opacity effects on the lines. The spectrum with opacity effects ("thick") has been offset by +50 mÅ.

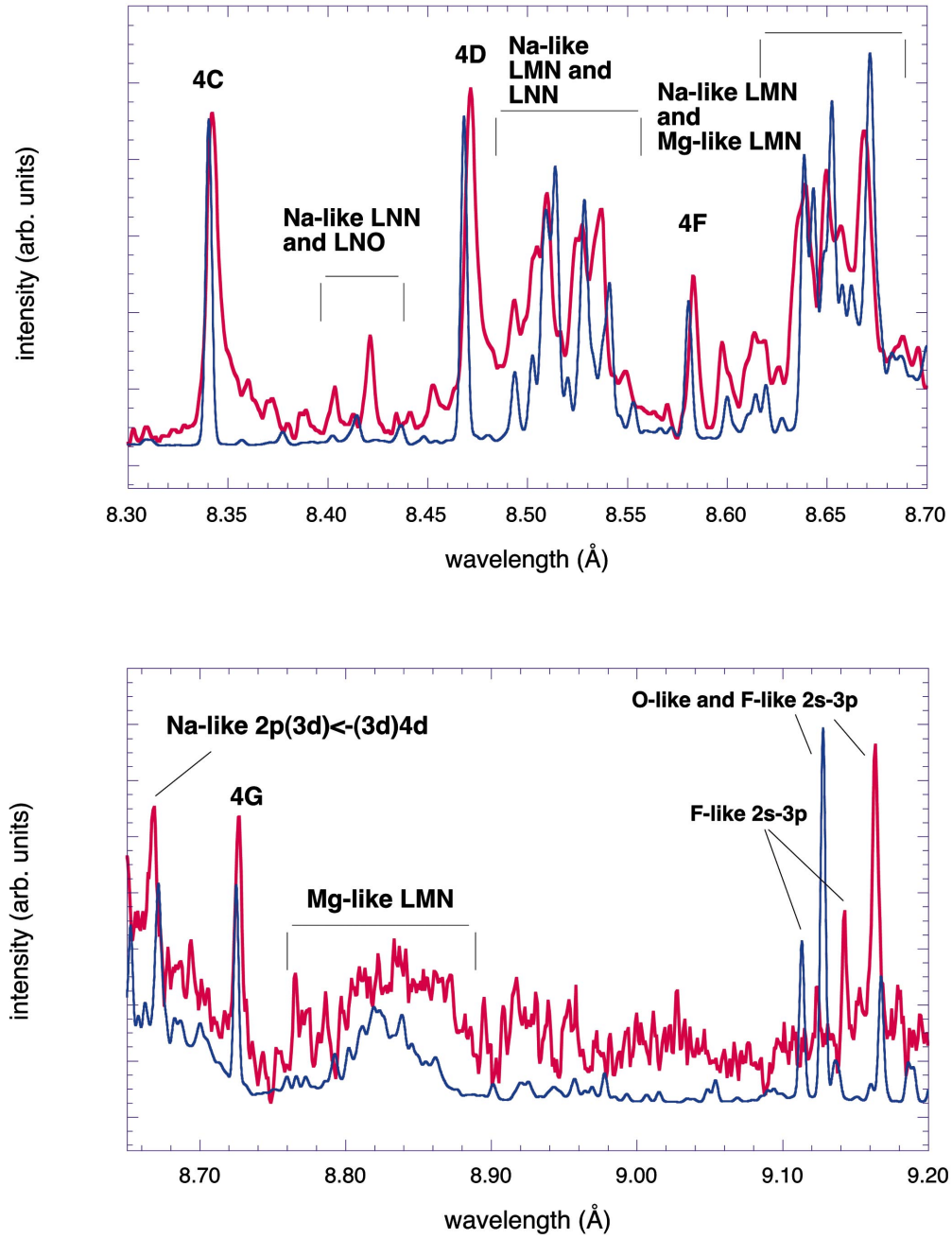

FIG. 8. (Color) Spectrum in the range of the $n=4$ Zn XXI resonance lines with strong dielectronic Rydberg satellites (top: 15 ns Nd:glass LPP, bottom: 12 ns XeCl LPP data—blue). CR model results (pink) with full spectra of DR channels overlaid; optical depths with $L=200$ μm have been computed for the O-, F- and Ne-like resonance lines.

the initial state of the recombining ion and where all the temperature dependence is contained in

$$F_1(T_e) = \frac{1}{2}\left(\frac{4\pi a_0^2\ \mathrm{Ry}}{T_e}\right)^{3/2} \exp\left(-\Delta E_{i,j}/T_e\right), \qquad (8)$$

where a_0 is the Bohr radius, Ry is the Rydberg unit of energy and $\Delta E_{i,j}$ is the capture energy of the free electron, i.e., the energy difference between the initial level of the recombining ion, Ne- or Na-like, and a doubly excited level of the recombined ion. The satellite-intensity factor due to DR from level i of ion $(q+1)$ via level j of ion q to level f is given by

$$F_2(j,f) = \frac{g_j}{g_i} A_{j,i}^{AI} \beta_{j,f}, \qquad (9)$$

where the g's are the statistical weights of the intermediate (autoionizing) and initial (recombining) levels, and $A_{j,i}^{AI}$ is the rate of autoionization from level j to level i, and $\beta_{j,f}$ is the radiative branching ratio from the upper level of the observed transition:

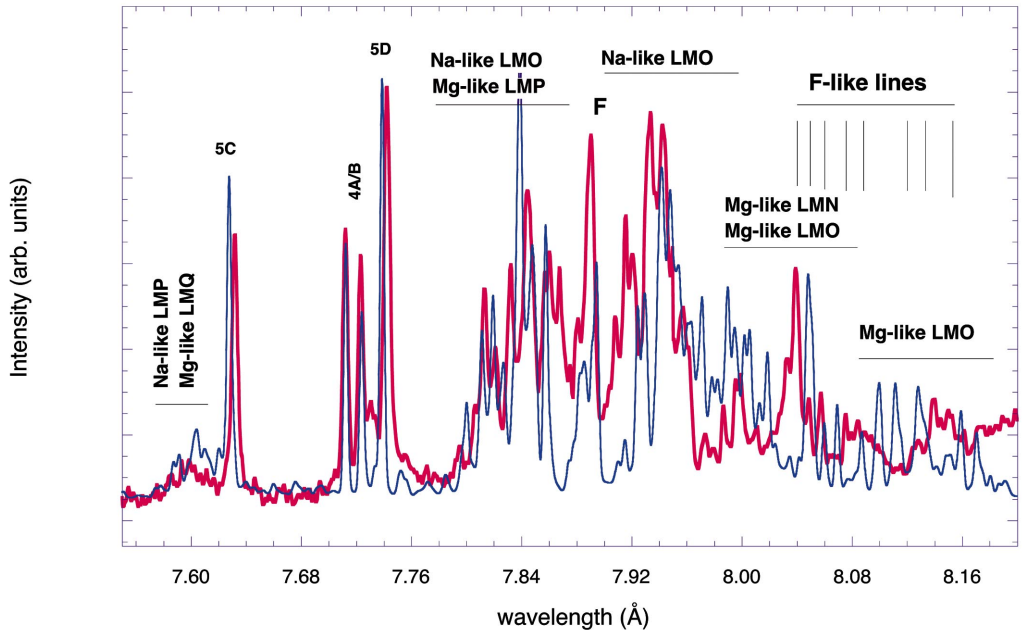

FIG. 9. (Color) Spectrum in the range of the $n=5$ Zn XXI resonance lines with strong dielectronic Rydberg satellites (15 ns Nd:glass LPP data—blue). CR model results (pink) with full spectra of DR channels overlaid; optical depths with $L=50$ μm have been computed for the O-, F- and Ne-like resonance lines.

$$\beta_{j,f}=\frac{A_{j,f}}{\Sigma_{i'}A^{AI}_{j,i'}+\Sigma_{f'}A_{j,f'}}. \tag{10}$$

The sum over i' in Eq. (10) runs over all levels in the next higher ion reachable from level j by autoionization, and the sum over f' runs over all bound levels reachable from j by radiative decay. The values of $A_{j,f}$ and $F_2(j,f)$ for each component of the numbered transition in Figs. 2 and 3 are given in Table II.

The results of our CR calculations for the Rydberg DR satellites to Zn XXI lines are shown in Figs. 4 and 5. The LMN and LMO traces in Figs. 4 and 5 show that there are some global features to each spectrum. For each LMn'' channel, there are always three distinct bands of emission. These bands are due to the promotion of a $2s$, $2p_{1/2}$ or $2p_{3/2}$ electron, in order of increasing wavelength, during the radiationless capture event. Only the highest energy $2s$-promotions for the LMM channel fall in the spectral window in both figures. The $2s$ features in the LMM channel and the LNO spectra have been artificially enhanced by the normalization of each spectrum in Figs. 4 and 5 and contribute little to the data in Figs. 1–3. The LNn'' channels also show emission in three distinct spectral regions based on the promotion of the $n=2$ electron, but both $2p_j$ features are also split, based on whether stabilization of the autoionizing state proceeds via $4s\rightarrow 2p$ (longer wavelength) or $4d\rightarrow 2p$ (shorter wavelength). These considerations are visible in the Mg-like LNO spectrum in Fig. 6, where the spectrum has been resolved based on the value of the $3\ell'$ spectator electron. In this case, the DR events proceed as: $(2\ell)^8 3\ell' + e \rightarrow (2\ell)^7 3\ell' 4\ell'' 5\ell'''$ $\rightarrow$ stable Mg-like level $+h\nu$, where $h\nu$ is the photon emitted during the stabilizing transition. The spectral bands characteristic of the $2s$ and $2p_j$ promotions are clearly visible, the contribution of the channel with a $3s$ spectator, which originates from the Na-like ground level, is negligible compared to the other two 3ℓ-spectator contributions (note logarithmic ordinate). The splitting of each $2p_j$ promotion based on the stabilization of the $4\ell''$ electron is also visible.

C. Line opacities

In our data, the $n=4$ and $n=5$ Zn XXI lines are affected by large optical depths. The optical depth (neglecting stimulated emission) in a line with frequency ν is given by the line opacity multiplied by the number density of absorbing ions and integrated along the line of sight through the plasma: $\tau(\nu)=\kappa_\nu N_l L$, where

$$\kappa_\nu=\frac{e^2}{mc^2}f_{l,u}\left(\frac{\pi Mc^2}{2k_BT_i}\right)^{1/2},$$

$$\times\lambda\phi(\nu)=(1.53\times 10^{-24})\frac{g_uA_{u,l}}{g_l(\Delta E)^3}\left(\frac{\mu}{T_i}\right)^{1/2}\phi(\nu), \tag{11}$$

where e and m are the electron mass and charge, M is the absorbing ion mass, c and k_B are the speed of light and Boltzmann's constant, $f_{l,u}$ is the absorption oscillator strength for the line in question, λ is the transition wavelength, and $\phi(\nu)$ is the normalized line profile. Equivalently, κ_ν is given by the right-hand expression with the ion mass μ in units of proton mass, T_i in eV, and the transition energy ΔE in hartrees (=2 Ry). Atomic data for the Zn^{20+} $n=4,5$ resonance lines and the strongest Zn^{19+} satellites are given in Table III for two cases ($N_e=10^{21}$ cm^{-3}, $L=200$ μm and $N_e=10^{22}$ cm^{-3}, $L=100$ μm), and assuming $\phi(\nu_0)=0.5$ for a reasonably narrow line at line center. The nC and nD lines are

TABLE II. Data for selected features observed in the spectral range of the $n=4$ and $n=5$ Zn XXI resonance lines. Each Zn XX and Zn XIX feature comprises several blended transitions. The key number corresponds to Figs. 2 and 3. The ion indicated is the recombined ion that makes the spectral feature. Numbers in braces represent powers of ten, i.e., X.XX[+Y]=X.XX$\times 10^{Y}$.

Key	Ion	Lower level	Upper level	J_l	J_u	λ_{calc} (Å)	$g_u A_{u,l}$ (s^{-1})	F_2 (s^{-1})
			$5\rightarrow 2$ DR channels					
100	19-LMO	$2s^2 2p^6 3p_{1/2}$	$2s^2 2p_{1/2}^2 2p_{3/2}^3 3p_{3/2} 5d_{3/2}$	1/2	3/2	7.9239	9.52[+11]	7.67[+11]
	19-LMO	$2s^2 2p^6 3s_{1/2}$	$2s^2 2p_{1/2}^2 2p_{3/2}^3 3s 5d_{5/2}$	1/2	3/2	7.9244	2.10[+13]	3.04[+11]
101	19-LMO	$2s^2 2p^6 3p_{3/2}$	$2s^2 2p_{1/2}^2 2p_{3/2}^3 3p_{3/2} 5d_{5/2}$	3/2	5/2	7.9283	1.55[+13]	1.04[+12]
	19-LMO	$2s^2 2p^6 3p_{3/2}$	$2s^2 2p_{1/2}^2 2p_{3/2}^3 3p_{3/2} 5d_{5/2}$	3/2	5/2	7.9297	7.91[+12]	3.15[+12]
	19-LMO	$2s^2 2p^6 3s_{1/2}$	$2s^2 2p_{1/2}^2 2p_{3/2}^3 3s 5d_{3/2}$	1/2	1/2	7.9311	7.04[+12]	1.13[+10]
	19-LMO	$2s^2 2p^6 3p_{3/2}$	$2s^2 2p_{1/2}^2 2p_{3/2}^3 3p_{3/2} 5d_{3/2}$	3/2	1/2	7.9311	7.05[+12]	2.97[+12]
102	19-LMO	$2s^2 2p^6 3s_{1/2}$	$2s^2 2p_{1/2}^2 2p_{3/2}^3 3s 5d_{5/2}$	1/2	1/2	7.9366	4.95[+12]	9.00[+11]
	19-LMO	$2s^2 2p^6 3p_{1/2}$	$2s^2 2p_{1/2}^2 2p_{3/2}^3 3p_{1/2} 5d_{5/2}$	1/2	1/2	7.9389	9.48[+12]	3.80[+12]
	19-LMO	$2s^2 2p^6 3s_{1/2}$	$2s^2 2p_{1/2}^2 2p_{3/2}^3 3s 5d_{5/2}$	1/2	3/2	7.9397	4.08[+12]	5.77[+11]
	19-LMO	$2s^2 2p^6 3p_{1/2}$	$2s^2 2p_{1/2}^2 2p_{3/2}^3 3p_{1/2} 5d_{5/2}$	1/2	3/2	7.9405	1.68[+13]	1.21[+13]
	19-LMO	$2s^2 2p^6 3p_{3/2}$	$2s^2 2p_{1/2}^2 2p_{3/2}^3 3p_{3/2} 5d_{5/2}$	3/2	3/2	7.9422	1.34[+13]	2.57[+12]
	19-LMO	$2s^2 2p^6 3p_{3/2}$	$2s^2 2p_{1/2}^2 2p_{3/2}^3 3p_{3/2} 5d_{5/2}$	3/2	1/2	7.9422	4.79[+12]	3.79[+12]
	19-LMO	$2s^2 2p^6 3p_{3/2}$	$2s^2 2p_{1/2}^2 2p_{3/2}^3 3p_{3/2} 5d_{5/2}$	3/2	5/2	7.9434	1.19[+13]	9.76[+21]
103[a]	19-LMO	$2s^2 2p^6 3d_{3/2}$	$2s^2 2p_{1/2}^2 2p_{3/2}^3 3d_{5/2} 5d_{5/2}$	3/2	1/2	7.9457	2.04[+12]	7.74[+07]
	19-LMO	$2s^2 2p^6 3d_{5/2}$	$2s^2 2p_{1/2}^2 2p_{3/2}^3 3d_{5/2} 5d_{5/2}$	5/2	7/2	7.9461	2.21[+13]	1.71[+13]
	19-LMO	$2s^2 2p^6 3d_{3/2}$	$2s^2 2p_{1/2}^2 2p_{3/2}^3 3d_{5/2} 5d_{5/2}$	3/2	5/2	7.9465	4.36[+11]	2.29[+11]
	19-LMO	$2s^2 2p^6 3p_{3/2}$	$2s^2 2p_{1/2}^2 2p_{3/2}^3 3p_{3/2} 5d_{5/2}$	3/2	3/2	7.9471	4.91[+11]	5.28[+10]
	19-LMO	$2s^2 2p^6 3d_{3/2}$	$2s^2 2p_{1/2} 2p_{3/2}^4 3d_{3/2} 5s$	3/2	3/2	7.9478	1.07[+12]	4.85[+11]
	19-LMO	$2s^2 2p^6 3d_{5/2}$	$2s^2 2p_{1/2}^2 2p_{3/2}^3 3d_{5/2} 5d_{3/2}$	5/2	3/2	7.9482	9.00[+12]	2.27[+12]
	19-LMO	$2s^2 2p^6 3d_{3/2}$	$2s^2 2p_{1/2}^2 2p_{3/2}^3 3d_{5/2} 5d_{3/2}$	3/2	5/2	7.9482	7.64[+11]	3.84[+12]
	19-LMO	$2s^2 2p^6 3d_{3/2}$	$2s^2 2p_{1/2}^2 2p_{3/2}^3 3d_{3/2} 5d_{3/2}$	3/2	3/2	7.9490	4.27[+12]	1.77[+12]
	19-LMO	$2s^2 2p^6 3p_{3/2}$	$2s^2 2p_{1/2}^2 2p_{3/2}^3 3p_{3/2} 5d_{3/2}$	3/2	5/2	7.9496	2.05[+12]	1.79[+12]
	19-LMO	$2s^2 2p^6 3d_{5/2}$	$2s^2 2p_{1/2}^2 2p_{3/2}^3 3d_{5/2} 5d_{5/2}$	5/2	5/2	7.9507	1.14[+13]	5.96[+12]
			$4\rightarrow 2$ DR channels					
128	19-LMN	$2s^2 2p^6 3p_{3/2}$	$2s^2 2p_{1/2} 2p_{3/2}^4 3p_{3/2} 4d_{3/2}$	3/2	5/2	8.5141	5.09[+13]	3.87[+13]
	19-LMN	$2s^2 2p^6 3p_{3/2}$	$2s^2 2p_{1/2} 2p_{3/2}^4 3p_{3/2} 4d_{3/2}$	3/2	3/2	8.5150	1.59[+13]	4.45[+11]
	19-LNN	$2s^2 2p^6 4f_{7/2}$	$2s^2 2p_{1/2}^2 2p_{3/2}^3 4d_{5/2} 4f_{5/2}$	7/2	9/2	8.5122	3.40[+13]	7.63[+11]
	19-LNN	$2s^2 2p^6 4f_{7/2}$	$2s^2 2p_{1/2}^2 2p_{3/2}^3 4d_{5/2} 4f_{5/2}$	7/2	7/2	8.5144	5.07[+13]	2.58[+12]
130	19-LMN	$2s^2 2p^6 3d_{5/2}$	$2s^2 2p_{1/2} 2p_{3/2}^4 3d_{5/2} 4d_{3/2}$	5/2	7/2	8.5380	2.82[+13]	2.08[+13]
	19-LMN	$2s^2 2p^6 3d_{5/2}$	$2s^2 2p_{1/2}^2 2p_{3/2}^3 3d_{3/2} 4d_{3/2}$	5/2	5/2	8.5411	3.54[+13]	2.56[+13]
	19-LMN	$2s^2 2p^6 3d_{3/2}$	$2s^2 2p_{1/2} 2p_{3/2}^4 3d_{3/2} 4d_{3/2}$	3/2	5/2	8.5418	2.02[+13]	1.74[+13]
	19-LNN	$2s^2 2p^6 4d_{5/2}$	$2s^2 2p_{1/2} 2p_{3/2}^4 4d_{3/2} 4d_{5/2}$	5/2	5/2	8.5387	5.22[+13]	3.46[+12]
	19-LNN	$2s^2 2p^6 4p_{3/2}$	$2s^2 2p_{1/2}^2 2p_{3/2}^3 4p_{3/2} 4d_{5/2}$	3/2	3/2	8.5417	2.75[+13]	3.63[+12]
136[b]	19-LMN	$2s^2 2p^6 3d_{3/2}$	$2s^2 2p_{1/2}^2 2p_{3/2}^3 3d_{5/2} 4d_{5/2}$	3/2	3/2	8.6695	1.07[+13]	2.84[+12]
	19-LMN	$2s^2 2p^6 3d_{5/2}$	$2s^2 2p_{1/2}^2 2p_{3/2}^3 3d_{5/2} 4d_{5/2}$	5/2	5/2	8.6706	3.32[+13]	2.74[+13]
	19-LMN	$2s^2 2p^6 3d_{5/2}$	$2s^2 2p_{1/2}^2 2p_{3/2}^3 3d_{3/2} 4d_{3/2}$	5/2	7/2	8.6718	3.26[+13]	3.11[+13]
	19-LMN	$2s^2 2p^6 3d_{3/2}$	$2s^2 2p_{1/2}^2 2p_{3/2}^3 3d_{3/2} 4d_{5/2}$	3/2	5/2	8.6722	2.20[+13]	1.81[+13]
	19-LMN	$2s^2 2p^6 3p_{3/2}$	$2s^2 2p_{1/2}^2 2p_{3/2}^3 3p_{3/2} 4d_{5/2}$	3/2	5/2	8.6727	4.98[+12]	4.05[+12]
	19-LMN	$2s^2 2p^6 3p_{3/2}$	$2s^2 2p_{1/2}^2 2p_{3/2}^3 3p_{3/2} 4d_{5/2}$	3/2	3/2	8.6727	2.42[+12]	2.27[+11]
	19-LMN	$2s^2 2p^6 3d_{3/2}$	$2s^2 2p_{1/2}^2 2p_{3/2}^3 3d_{3/2} 4d_{5/2}$	3/2	3/2	8.6735	1.39[+13]	4.14[+11]
	19-LMN	$2s^2 2p^6 3d_{5/2}$	$2s^2 2p_{1/2}^2 2p_{3/2}^3 3d_{5/2} 4d_{5/2}$	5/2	3/2	8.6745	1.27[+13]	3.37[+12]

[a]Also blended with two F-like transitions at 7.9483 and 7.9519 [19].
[b]Also blended with Mg-like LMN features.

TABLE III. Estimated optical depths on Ne- and Na-like Zn^{20+} and Zn^{19+} x-ray lines. Columns are transition wavelengths considered, calculated radiative decay rates, and the optical depths at line center for $N_e=10^{21}$ cm^{-3}, $L=200$ μm(*i*), and $N_e=10^{22}$ cm^{-3}, $L=100$ μm (*ii*), ion densities and level populations have been computed at $T_e=200$ eV. The optical depths for the Zn XX features are summed over all transitions listed in Table II. For the wavelengths, the Zn^{20+} observed values from [15] are used, for Zn^{19+}, the centroid of the emitting feature from our CR calculation is listed, wavelengths and A-rates for the individual components of each Na-like feature are in Table II. Numbers in parentheses represent powers of ten.

Label	λ (Å)	$g_uA_{u,l}$ (s^{-1})	$\tau(\nu_0)$	
			i	*ii*
5C	7.6309	1.48[+13]	18.2	53.5
5D	7.7421	2.67[+13]	34.4	100.8
5G	7.8460	1.31[+12]	1.8	5.1
100	7.9238		0.3	1.5
101	7.9297		0.4	2.2
102	7.9402		0.6	3.8
103	7.9485		0.4	2.3
4A	7.7124	8.76[+12]	11.1	32.7
4B	7.7239	4.41[+12]	5.6	16.5
4C	8.3420	3.68[+13]	59.3	173.9
4D	8.4715	4.08[+13]	68.8	201.9
4F	8.5828	1.74[+12]	3.1	9.0
4G	8.7270	2.21[+12]	4.1	12.0
128	8.5141		0.8	4.6
130	8.5409		0.7	4.3
136	8.6718		1.2	7.3

very optically thick in both cases. The effects of these optical depths on the plasma [16] are that the average charge state of the plasma is driven higher by enhanced ionization from more-highly-populated Zn^{20+} upper levels, thus enhancing F-like and O-like spectral lines, and that the relative strength of the weaker Zn XXI lines are enhanced by collisionally coupling the upper states of 4C and 4D to the upper states of 4F and 4G. Figure 7 shows the computed spectra from O-, F- and Ne-like Zn in the range of the $n=4$ Zn XXI resonance lines, with and without escape factors. For this figure, $T_e=T_i=300$ eV, $N_e=10^{21}$ cm^3, the ion level populations are computed self-consistently, and the plasma is assumed to have uniform density and temperature with $L=200$ μm. The enhanced F-like and 4F, 4G emission is clearly visible in the escape factors calculation.

IV. SPECTRAL IDENTIFICATIONS

As is shown below (Sec. V), in the case of a Zn target, the Na- and Mg-like Rydberg satellites can be important or dominant for $T_e \leqslant 300$ eV. In the present experiments we have demonstrated that Rydberg satellites can be produced in LPPs. In other experiments, such as with the ps-pulse length laser at intensities $\approx 10^{17}$ W/cm^2 (see Fig. 1 in Ref. [19]) some of the satellite lines presented here can mask O- and F-like lines, thus giving errors in plasma parameter measurements. Further, in the case of ps or sub-ps experiments, strong inhomogeneities in both temporal (i.e., laser prepulse) or spatial (i.e., strong temperature gradients) conditions can give rise to errors in plasma parameter measurements. For our experimental conditions, in which we tried to maximize the concentration of Na- and Mg-like satellites, we do not expect T_e or N_e conditions to vary much. Indeed, we find satisfactory agreement between observed spectra and our models for a single set of temperature-density conditions. However, there is strong variation in the computed optical depths on Ne-like resonance lines for the different LPPs; this is consistent with the different spatial scales of the LPPs observed here.

As we have pointed out previously [15,19], many spectral features observed in the nanosecond LPP are satellites to the Zn XXI spectral lines, caused by radiative transitions from highly excited autoionizing states of Mg- and Na-like ions. Simulating these features is a computationally challenging task due to the enormous number of autoionizing levels that must be considered. Generally speaking, such features can be intense relative to Zn XXI lines only in a plasma with $T_e<250$ eV. However, we also see lines from spectra of ions more highly charged than Zn^{20+}; spatial non-uniformity of the laser flux across the focal spot may lead to hot spots that emit the lines from F- and O-like Zn^{21+} and Zn^{22+} ions. Since our data are spatially integrated across the face of the laser spot, we pick-up the contribution of these hot spots. Further, our data are integrated in time over the whole experiment, thus there is no way to determine if the lines from high and low charge states are temporally coincident.

Figure 8 shows the satellite spectral structures in the vicinity of the $n=4$ Zn XXI resonance lines for the same spectra as in Fig. 2. The data in both panels have been modeled assuming $T_e=250$ eV, $N_e=10^{21}$ cm^{-3}, and optical depths on all lines computed for an $L=200$ μm plasma. The good agreement in the relative strength of the 4F line to the 4C and 4D lines indicates that these assumptions are reasonable for the 12 ns Nd:glass LPP. Satellite channels that are visible are the Na-like LMN and the Mg-like LMN on the long-wavelength side of 4D, Na-like LNN between 4C and 4D, and the bulk of the Mg-like LMN channel in the lower panel of Fig. 8. We note that $n=3$ to $n=2$ F-like Zn XXII lines are visible at the longest wavelengths in the XeCl LPP spectrum, we have not carried out extensive analysis of the $n=3$ to $n=2$ Zn x-ray transitions here or previously.

Figure 9 shows the spectrum in the range of the $n=5$ Zn XXI resonance lines with strong dielectronic Rydberg satellites (from Fig. 3). The data from thisNd:glass LPP have been modeled assuming $T_e=250$ eV, $N_e=10^{21}$ cm^{-3}, and optical depths on all lines computed for a $L=50$ μm plasma. The Na- and Mg-like LMO satellite spectra dominate the features near the parent $n=5$ Zn XXI lines. The higher-n Mg-like LMP also appear on the long-wavelength side of the 5D line, while the Na-like LMP and Mg-like LMQ features appear on the blue side of 5C. Also appearing in Fig. 9 are

previously identified [19] F-like lines, $4d \rightarrow 2p$ transitions at 7.8865 and 8.0435 Å. The presence of satellite features on both the red and blue sides of the Zn XXI resonance lines emphasizes the point that using broadened line profiles for diagnostics in dense plasmas requires careful attention to the contribution from Rydberg satellite transitions.

The march to still higher-n is shown for the Na- and Mg-like Rydberg satellites in Fig. 10, which overlaps with the range covered in Fig. 9. The data from this XeCl LPP have been modeled assuming $T_e = 250$ eV, $N_e = 10^{21}$ cm^{-3}, and optical depths on all lines computed for an $L = 200$ μm plasma. The energy of a given Ne-like transition is seen to be increasing faster than the transition energy for Na- and Mg-like satellites with the same n. Thus, the Na-like LMP and LMQ satellite features both appear on the red side of 6D. Also of note in the figure is Na-like LMO satellite feature that proceeds through the promotion of (stabilization to) a $2s$ electron (hole). As was mentioned in Sec. III B, this LMO channel is higher in energy than are the LMO channels that stabilize through decays to a $2p$ vacancy. Also labeled in Fig. 10 are three previously identified F-like transitions at 7.4390, 7.3279 and 7.2396 Å [19]. Features labeled with a number and identified in Figs. 8 and 9 are identified in Table I.

V. DIAGNOSTIC UTILITY

Figure 11 shows the T_e dependence in the Na-, Ne-, F- and O-like spectra in the range of the Zn XXI 4C and 4D lines (right panel) and 5C and 5D lines (left panel). These models only have Mg- and Na-like satellites for $n \leqslant 5$ (hence, no Rydberg satellite features for Zn XXI lines with $n \geqslant 6$). The Na-like satellites remain strong for temperatures up to 300 eV, the F- and O-like lines begin to dominate for $T_e \geqslant 300$ eV. This is particularly true in the left panel, where the 2–4 O-like and 2–4 and 2–5 F-like transitions appear between 7.2 and 8.2 Å [19]. The O-like $2s-3p$ transitions appear in the highest temperature traces in the right panel of Fig. 11. The Zn XXI lines are optically thick for $T_e \leqslant 400$ eV, after which point the Ne-like abundance is too low for there to be strong opacity effects on these lines. The effects of opacity can be seen on the 4F and 4G lines. From case i in Table III, it is seen that for $N_e \lesssim 10^{21}$ cm^{-3} the Na-like satellite features are optically thin. Thus, if the ions that emit the satellite features are spatially localized near the laser-interaction region, the Rydberg satellites can serve as a local diagnostic of conditions, as in [14].

VI. CONCLUSION

High-spectral-resolution observations have been made of Zn LPPs. Spectra have been recorded from three types of LPPs, which were made by lasers with pulse lengths that differed by four orders of magnitude. Wavelength measurements were accomplished with K-shell reference lines in the same spectral range, and with previously identified Zn XXI resonance lines. The plasmas of the present work are dominated by strong satellite features emitted by Na- and Mg-like Zn^{19+} and Zn^{18+}. These satellite features are excited principally by dielectronic recombination of the Ne- or Na-like ions. Detailed collisional-radiative modeling of these satellite features reveals the origin of systematic behavior in the spectral distribution of the emitted x rays. In particular, well-

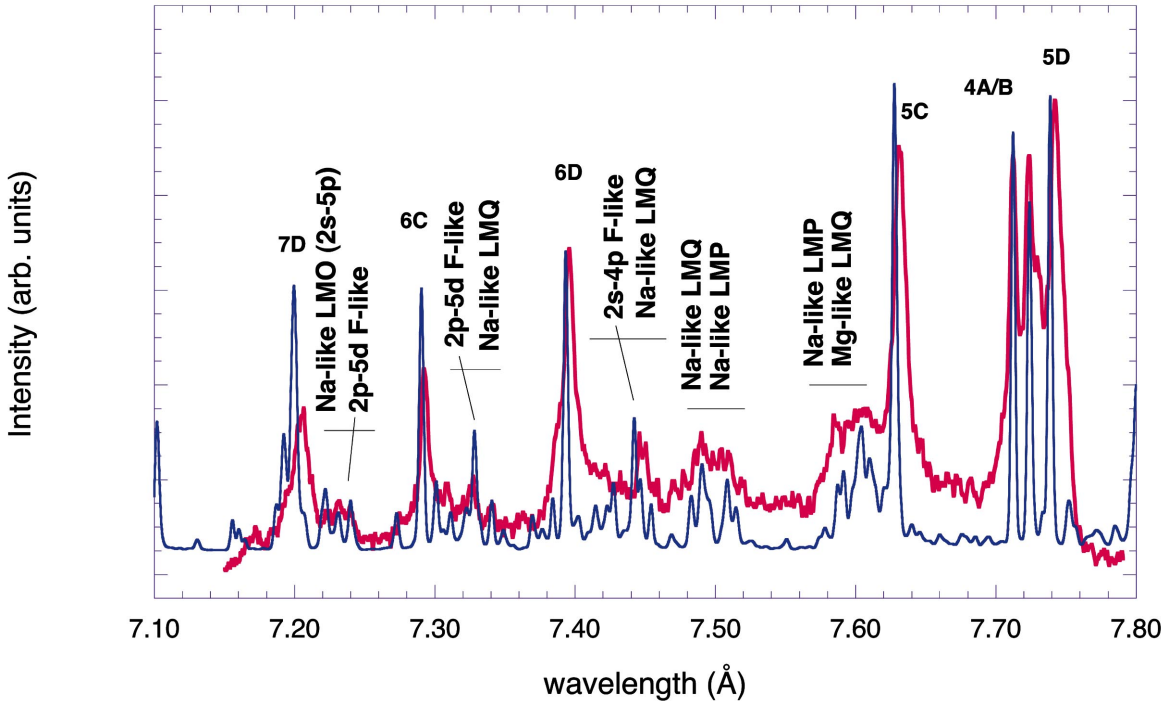

FIG. 10. (Color) Spectrum in the range of the $n = 5-7$ Zn XXI resonance lines with strong dielectronic Rydberg satellites (10 ns XeCl LPP data—blue). CR model results (pink) with full spectra of DR channels overlaid; optical depths with $L = 200$ μm have been computed for the O-, F- and Ne-like resonance lines.

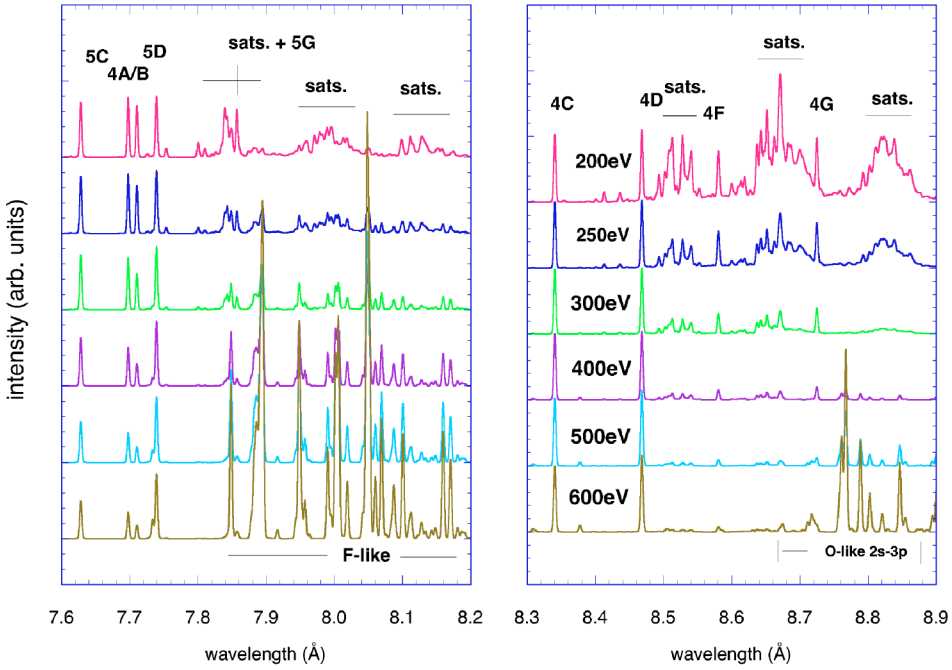

FIG. 11. (Color online) Spectra in the range of the $n=4$ (right) and $n=5$ (left) Zn XXI resonance lines with strong dielectronic Rydberg satellites for different electron temperatures. All spectra have been computed at $N_e=10^{21}$ cm^{-3}, with optical depths computed for $L=200$ μm.

resolved bunches of lines appear for each n-resolved manifold of autoionizing channels based on the jj-coupled L-shell electron ($2s$, $2p_{1/2}$ and $2p_{3/2}$) promoted during recombination.

The laser-produced Zn spectra shown above have features that arise from enormous manifolds of dielectronic-recombination-fed satellites to the Zn XXI resonance lines. These satellite features converge to the red edge of the parent line, particularly for the $n=4$ Zn XXI lines. Any simulation of Stark broadened line profiles for high-n members of the Ne-like nC and nD series will have to account for the large contribution of these satellites to the broadened line shape if accurate diagnostic information is to be obtained. Our CR models show that for Zn($Z=30$) the Rydberg satellites must be considered for plasmas with $T_e \lesssim 300$ eV; for higher-Z elements of interest to ICF plasmas, such as Xe [12], the Rydberg satellites will be important in plasmas with significantly higher temperatures.

The Zn XXI $n=4$ lines are optically thick for the laser-irradiation conditions explored here, the $n=5$ lines also have large optical depths. Thus, direct probing of plasma conditions near the laser-interaction region will be complicated by the difficulty in modeling the transport of these lines. However, the Na-like satellites to these transitions are estimated to be optically thin in the present work. Thus, spatially resolved observations in this spectral range could use the Rydberg satellites as local probes of the laser-target-interaction region. Such spatially resolved measurements have yet to be done for L-shell emitting ions, we hope to see this kind of work done in the near future.

ACKNOWLEDGMENTS

This work was performed under the auspices of the U.S. Department of Energy by University of California Lawrence Livermore National Laboratory under Contract No. W-7405-Eng-48. This work was also partly supported by ISTC projects Nos. 1785 and 2155. The authors wish to thank Dr. M. Chen and Dr. S. Hansen at LLNL for useful discussions.

[1] H. R. Griem, *Spectral Line Broadening by Plasmas* (Academic, New York, 1974), Chap. 2.
[2] R. C. Mancini, A. S. Shlyaptseva, P. Audebert, J. P. Geindre, S. Bastiani, J.-C. Gauthier, G. Grillon, A. Mysyrowicz, and A. Antonetti, Phys. Rev. E **54**, 4147 (1996).
[3] M. M. Murnane, H. C. Kapteyn, and R. W. Falcone, Phys. Rev. Lett. **62**, 155 (1989).
[4] A. Zigler, P. G. Burkhalter, D. J. Nagel, M. D. Rosen, K. Boyer, G. Gibson, T. S. Luk, A. McPherson, and C. K. Rhodes, Appl. Phys. Lett. **59**, 534 (1991).
[5] Z. Jiang, J. C. Kieffer, J. P. Matte, M. Chaker, O. Peyrusse, D. Gilles, G. Korn, A. Maksimchuk, S. Coe, and G. Mourou, Phys. Plasmas **2**, 1702 (1995).
[6] B. K. F. Young, B. G. Wilson, D. F. Price, and R. E. Stewart, Phys. Rev. E **58**, 4929 (1998).
[7] K. B. Fournier, B. K. F. Young, S. J. Moon, M. E. Foord, D. F. Price, R. L. Shepherd, and P. T. Springer, J. Quant. Spectrosc. Radiat. Transf. **71**, 339 (2001).
[8] U. Andiel, K. Eidmann, P. Hakel, R. C. Mancini, G. C. Junkel-Vives, J. Abdallah, and K. Witte, Europhys. Lett. **60**, 861 (2002).
[9] K. Eidmann, U. Andiel, F. Pisani, P. Hakel, R. C. Mancini, G. C. Junkel-Vives, J. Abdallah, and K. Witte, J. Quant. Spectrosc. Radiat. Transf. **81**, 133 (2003).

[10] P. Audebert, R. Shepherd, K. B. Fournier, O. Peyrusse, D. Price, R. W. Lee, P. Springer, J.-C. Gauthier, and L. Klein, Phys. Rev. E **66**, 066412 (2002).

[11] R. Shepherd, P. Audebert, H.-K. Chen, K. B. Fournier, O. Peyreusse, S. Moon, R. W. Lee, D. Price, L. Klein, J.-C. Gauthier, and P. Springer, J. Quant. Spectrosc. Radiat. Transf. **81**, 431 (2003).

[12] C. J. Keane, B. A. Hammel, A. L. Osterheld, and D. R. Kania, Phys. Rev. Lett. **72**, 3029 (1994).

[13] A. S. Shlyaptseva, S. B. Hansen, V. L. Kantsyrev, D. A. Fedin, N. Ouart, K. B. Fournier, and U. I. Safronova, Phys. Rev. E **67**, 026409 (2003).

[14] F. B. Rosmej, D. H. H. Hoffmann, M. Geißel, M. Roth, P. Pirzadeh, A. Ya. Faenov, T. A. Pikuz, I. Yu. Skobelev, and A. I. Magunov, Phys. Rev. A **63**, 063409 (2001).

[15] K. B. Fournier, A. Ya. Faenov, T. A. Pikuz, I. Yu. Skobelev, F. Flora, S. Bollanti, P. Di Lazzaro, D. Murra, A. Reale, L. Reale, G. Tomassetti, A. Ritucci, I. Bellucci, S. Martellucci, G. Petrocelli, V. S. Belyaev, V. I. Vinogradov, A. S. Kyrilov, and A. P. Matafonov, J. Quant. Spectrosc. Radiat. Transf. **81**, 167 (2003).

[16] K. B. Fournier, A. Ya. Faenov, T. A. Pikuz, I. Yu. Skobelev, V. S. Belyaev, V. I. Vinogradov, A. S. Kyrilov, A. P. Matafonov, I. Bellucci, S. Martellucci, G. Petrocelli, T. Auguste, S. Hulin, P. Monot, and P. D'Oliveira, Phys. Rev. E **67**, 016402 (2003).

[17] K. B. Fournier, A. Ya. Faenov, T. A. Pikuz, I. Yu. Skobelev, F. Flora, S. Bollanti, P. Di Lazzaro, D. Murra, A. Reale, L. Reale, G. Tomassetti, A. Ritucci, I. Bellucci, S. Martellucci, and G. Petrocelli, J. Phys. B **35**, 3347 (2002).

[18] V. S. Belyaev, V. I. Vinogradov, A. S. Kyrilov, A. I. Magunov, A. P. Matafonov, T. A. Pikuz, I. Yu. Skobelev, and A. Ya. Faenov, JETP **96**, 897 (2003).

[19] K. B. Fournier, A. Ya. Faenov, T. A. Pikuz, I. Yu. Skobelev, V. S. Belyaev, V. I. Vinogradov, A. S. Kyrilov, A. P. Matafonov, F. Flora, S. Bollanti, P. Di Lazzaro, D. Murra, A. Reale, L. Reale, G. Tomassetti, A. Ritucci, M. Francucci, S. Martellucci, and G. Petrocelli, J. Phys. B **36**, 3787 (2003).

[20] A. Ya. Faenov, S. A. Pikuz, A. I. Erko, B. A. Bryunetkin, V. M. Dyakin, G. V. Ivanenkov, A. R. Mingaleev, T. A. Pikuz, V. M. Romanova, and T. A. Shelkovenko, Phys. Scr. **50**, 333 (1994).

[21] T. A. Pikuz, A. Ya. Faenov, S. A. Pikuz, V. M. Romanova, and T. A. Shelkovenko, J. X-Ray Sci. Technol. **5**, 323 (1995).

[22] B. K. F. Young, A. L. Osterheld, D. F. Price, R. Shepherd, R. E. Stewart, A. Y. Faenov, A. I. Magunov, T. A. Pikuz, I. Y. Skobelev, F. Flora, S. Bollanti, P. DiLazzaro, T. Letardi, A. Grilli, L. Palladino, A. Reale, A. Scafati, and L. Reale, Rev. Sci. Instrum. **69**, 4049 (1998).

[23] A. Bar-Shalom, M. Klapisch, and J. Oreg, J. Quant. Spectrosc. Radiat. Transf. **71**, 169 (2001).

[24] T. Holstein, Phys. Rev. **72**, 1212 (1947).

[25] J. P. Apruzese, J. Quant. Spectrosc. Radiat. Transf. **34**, 447 (1985).

[26] Dimitri Mihalas, *Stellar Atmospheres* (Freeman, San Francisco, 1978), pp. 279–281.

[27] Numbers in the figures do not start with "1" because these figures are part of a larger mosaic figure that includes more lines at shorter wavelengths; this figure will be presented elsewhere.